JGR Solid Earth

RESEARCH ARTICLE
10.1029/2023JB026956

Simultaneous Inversion of Ocean Bottom Pressure and Electromagnetic Tsunami Records for the 2009 Samoa Earthquake

Hiiro Yokoi[1], Toshitaka Baba[2], Zhiheng Lin[3,4], Takuto Minami[5], Masato Kamiya[1], Akino Naitoh[1], and Hiroaki Toh[6]

[1]Graduate School for Sciences and Technology for Innovation, Tokushima University, Tokushima, Japan, [2]Graduate School of Technology, Industrial and Social Sciences, Tokushima University, Tokushima, Japan, [3]Division of Earth and Planetary Sciences, Graduate School of Science, Kyoto University, Kyoto, Japan, [4]Center for Data Assimilation Research and Applications, Joint Support-Center for Data Science Research, Tachikawa, Japan, [5]Department of Planetology, Faculty of Science, Kobe University, Hyogo, Japan, [6]Data Analysis Center for Geomagnetism and Space Magnetism, Graduate School of Science, Kyoto University, Kyoto, Japan

Key Points:

- Sea surface fluctuations converted from the electromagnetic data were as precise as ±5 mm
- Tsunami magnetic field data were successfully incorporated into a conventional tsunami waveform inversion scheme
- The inclusion of the effects of frequency dispersion, self-attraction, and loading was important in finite-fault inversion

Supporting Information:

Supporting Information may be found in the online version of this article.

Correspondence to:

T. Baba,
baba.toshi@tokushima-u.ac.jp

Citation:

Yokoi, H., Baba, T., Lin, Z., Minami, T., Kamiya, M., Naitoh, A., & Toh, H. (2023). Simultaneous inversion of ocean bottom pressure and electromagnetic tsunami records for the 2009 Samoa earthquake. *Journal of Geophysical Research: Solid Earth*, *128*, e2023JB026956. https://doi.org/10.1029/2023JB026956

Received 20 APR 2023
Accepted 9 JUN 2023

Author Contributions:

Conceptualization: Toshitaka Baba, Hiroaki Toh
Data curation: Zhiheng Lin, Takuto Minami, Hiroaki Toh
Formal analysis: Hiiro Yokoi, Zhiheng Lin, Takuto Minami, Masato Kamiya, Akino Naitoh
Funding acquisition: Toshitaka Baba, Hiroaki Toh
Investigation: Hiiro Yokoi, Toshitaka Baba, Zhiheng Lin, Takuto Minami, Masato Kamiya, Akino Naitoh, Hiroaki Toh

Abstract

This study presents tsunami inversion analyses that simultaneously use ocean-bottom pressure and ocean-bottom electromagnetic data along with an accurate tsunami propagation model to estimate the earthquake source model for the 2009 Samoa earthquake. This earthquake was a doublet event that occurred along a pair of normal and thrust faults. To the best of our knowledge, this joint inversion of pressure and electromagnetic data is unprecedented. The incorporation of electromagnetic data in the tsunami inversion analysis was relatively simple, and the inclusion of frequency dispersion, self-attraction, and loading effects in the tsunami propagation calculations allowed the use of tsunami waveforms recorded at distant locations, which improved the reliability of the solutions obtained. Our best source model indicated that the east-west extent of the plate-boundary slip area was approximately 50 km, which is narrower than that of a previous fault model, and explained both electromagnetic and pressure data from the 2009 Samoa tsunami.

Plain Language Summary

On 29 September 2009, the 2009 Samoa earthquake occurred in the southern Pacific Ocean adjacent to the Tonga Trench subduction zone. This doublet earthquake was initiated as a normal-faulting event seaward of the trench axis, followed by a thrust-faulting event on the subduction zone interface close to the trench axis. An ocean bottom pressure gauge and magnetometers deployed in the South Pacific Ocean recorded the tsunami caused by the earthquake. Although tsunami inversion analysis generally uses ocean bottom pressure data alone, we employed ocean bottom electromagnetic data to estimate the slip area of this earthquake in this study. To the best of our knowledge, this is the first to join pressure and electromagnetic data were used jointly to yield an accurate slip model of the 2009 Samoa earthquake. We also considered wavelength dependence in the tsunami phase velocities to stabilize the inversion. Consequently, we found a slip area on the thrust fault that was shorter in the east-west direction than that estimated from the pressure and tide gauge data in previous studies.

1. Introduction

The Tonga Trench lies along the western margin of the Pacific Plate, where it subducts beneath the Australian Plate. The trench axis trends north-northeast in the south-central part of the trench; however, it swings abruptly to a west-northwesterly trend in the north. At 17:48:10 UTC on 29 September 2009, an Mw 8.1 earthquake occurred near the northern end of the Tonga Trench (hereafter, the 2009 Samoa earthquake). This earthquake was a doublet comprising normal slip beneath the outer rise and thrust slip on the subducting plate interface (Beavan et al., 2010; Duputel et al., 2012; Fan et al., 2016; Hossen et al., 2018; Lay et al., 2010; Nealy & Hayes, 2015). A slip first occurred on the normal fault, followed shortly by a slip on the thrust fault. According to Lay et al. (2010), the interval between the two events was 52 s, whereas Fan et al. (2016) and Nealy and Hayes (2015) have suggested shorter intervals (10–20 s).

The tsunami generated by the 2009 Samoa earthquake reached a run-up height of 22 m on a neighboring island, where 189 people were killed (Fritz et al., 2011; Okal et al., 2010). Tsunamis have been widely observed by the Deep-ocean Assessment and Reporting of Tsunamis (DART) network in the Pacific Ocean (Watada et al., 2014;

Methodology: Toshitaka Baba, Zhiheng Lin, Takuto Minami, Hiroaki Toh
Project Administration: Toshitaka Baba, Hiroaki Toh
Software: Toshitaka Baba
Supervision: Toshitaka Baba, Hiroaki Toh
Validation: Hiroaki Toh
Visualization: Toshitaka Baba
Writing – original draft: Hiiro Yokoi, Toshitaka Baba
Writing – review & editing: Toshitaka Baba, Zhiheng Lin, Takuto Minami, Hiroaki Toh

Zhou et al., 2012). Although several studies have proposed finite-fault models for the 2009 Samoa earthquake, none have accurately simulated the observed tsunami run-up (Bosserelle et al., 2020). Therefore, the finite-fault model of the 2009 Samoa earthquake requires further improvement.

In addition to conventional tsunami observations, data recorded by ocean bottom electromagnetometers (OBEMs) can be used to estimate finite-fault models. The dynamo effect (Faraday, 1832) causes a conductor moving in a background magnetic field to generate an electric field and current in a conductor, which in turn generates a secondary magnetic field. Because seawater is a good conductor, seawater movements associated with tsunami propagation generate a magnetic field (Tyler, 2005), which can be recorded by OBEMs. Thus, OBEM data provide information on both the height and direction of tsunami propagation (Lin et al., 2021; Sugioka et al., 2014; Zhang et al., 2014).

Toh et al. (2011) reported electromagnetic field data recorded by an OBEM in the northwestern Pacific Ocean during the tsunamis resulting from the 2006 and 2007 Kuril earthquakes, which were the first observations of tsunamis by OBEMs. Ichihara et al. (2013) used OBEM data recorded approximately 400 km off the coast of Japan to investigate the source area of the tsunami generated by the 2011 Tohoku earthquake. Kawashima and Toh (2016) applied nonnegative linear inversion to the OBEM data to estimate the slip distribution on the fault of the 2007 Kuril earthquake. However, their solution did not provide a comprehensive model because they used only OBEM data without the support of conventional tsunami data.

The electromagnetic data generated by the 2009 Samoa tsunami were recorded by a seafloor array for Tomographic Investigation by the seafloor ARray Experiment for the Society hotspot (TIARES network; Suetsugu et al., 2012) installed in the region bounded by latitude 17°–22°S and longitude 210°–220°E (Figure 1). The TIARES network consisted of an array of nine OBEMs (SOC1–SOC9), one of which (SOC8) was equipped with an ocean bottom pressure gauge (OBP). Lin et al. (2021) used the analytical solution derived by Minami et al. (2021) to obtain the sea level changes from magnetic field data recorded at SOC8 during the 2009 Samoa tsunami, which were consistent with those determined from the OBP data.

This study presents a finite-fault model for the 2009 Samoa earthquake that accurately simulates both OBEM data and hydrostatic pressure change recorded by OBP. Section 2 explains conversion methods from OBEM and OBP data to sea surface fluctuations. Section 3 performs a joint tsunami inversion using the converted data. Section 4 presents the obtained slip distributions with estimated errors. Section 5 discusses the applicability of OBEM data and the importance of tsunami calculation models through sensitivity analysis.

2. Data and Processing

2.1. Ocean Bottom Electromagnetic Data

The OBEMs of the TIARES array recorded the magnetic field variations caused by the tsunami resulting from the 2009 Samoa earthquake. The governing equation of the magnetic field induced by the motion of seawater in the Earth's magnetic field is given in the frequency domain as

$$\left(\nabla^2 + i\omega\sigma\mu_0\right)\boldsymbol{b} = -\sigma\mu_0\nabla\times(\boldsymbol{v}\times\boldsymbol{F}), \tag{1}$$

where $\boldsymbol{b} = (b_x, b_y, b_z)$, $\boldsymbol{v} = (v_x, v_y, v_z)$, and $\boldsymbol{F} = (F_x, F_y, F_z)$ are the tsunami-generated magnetic field, the velocity field of sea water, and the ambient geomagnetic field, respectively. ω, σ, and μ_0 are the angular frequency, electrical conductivity of the medium in concern, and magnetic permeability in a vacuum, respectively. In Equation 1, $\boldsymbol{b}$ and $\boldsymbol{v}$ were assumed ω-harmonic ($\propto e^{-i\omega t}$), and $\boldsymbol{F}$ can be assumed to be spatiotemporally constant for the analysis of a single site. Assuming a flat seafloor and constant tsunami propagation direction, we adopted the following expressions based on the linear dispersive wave equation to represent the tsunami horizontal velocity in the TIARES area (Minami et al., 2021):

$$\begin{cases} v_y = \eta\omega\dfrac{\cosh[k(z-H)]}{\sinh(kH)}e^{i(ky-\omega t)}, \\ v_z = -i\eta\omega\dfrac{\sinh[k(z-H)]}{\sinh(kH)}e^{i(ky-\omega t)}, \end{cases} \tag{2}$$

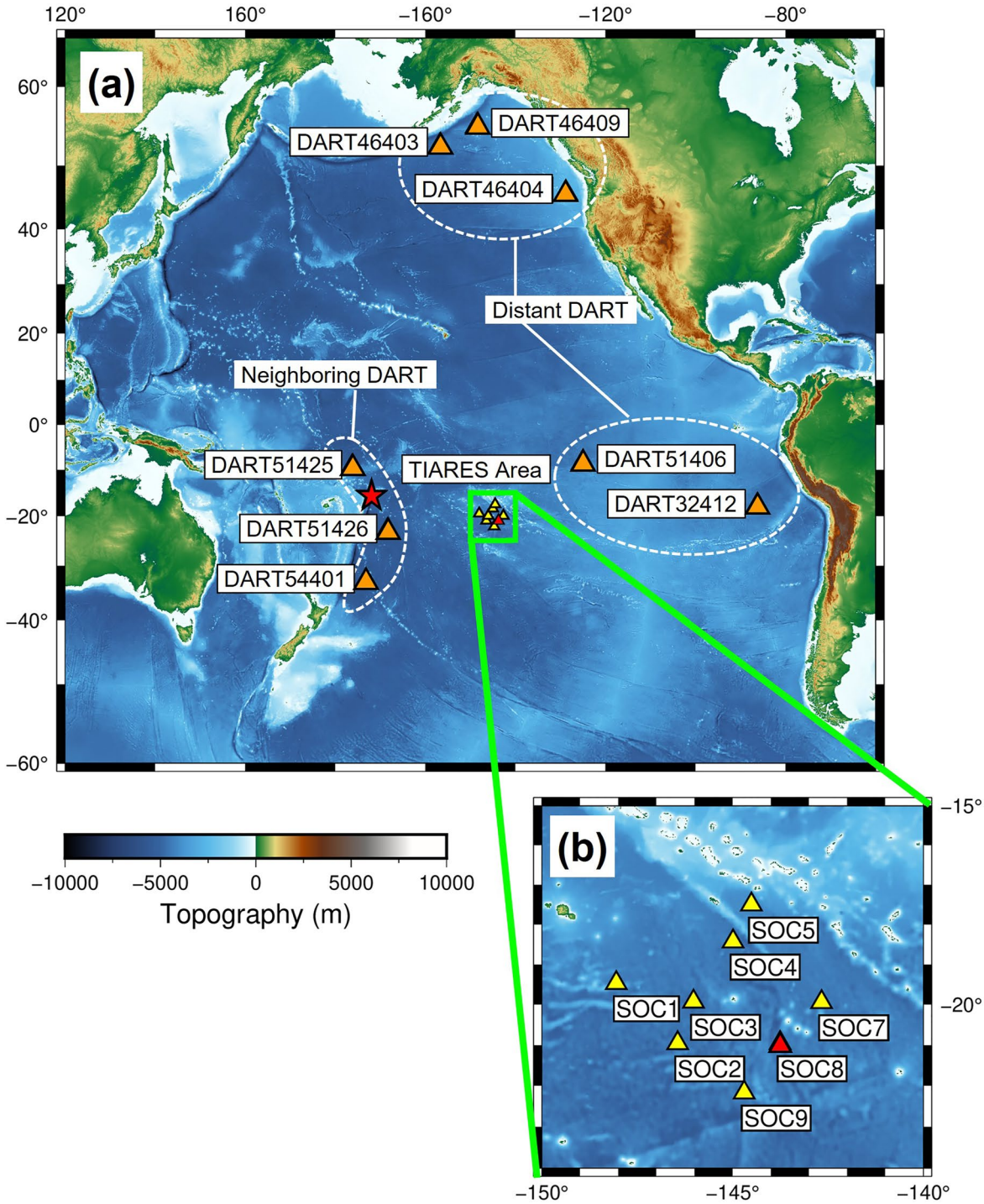

Figure 1. (a) Map showing the computational domain, tsunami stations, and the hypocenter of the 2009 Samoa earthquake (red star). DART stations (orange triangles) were equipped with OBP gauges. SOC stations (yellow triangles) of the TIARES seafloor array were equipped with OBEM gauges, but for SOC8 (red triangle) where a pair of OBP and OBEM was installed. (b) Enlarged map near the TIARES seafloor array. DART, Deep-ocean Assessment and Reporting of Tsunamis; OBEM, ocean bottom elecromagnetometer; OBP, ocean bottom pressure gauge; TIARES, Tomographic Investigation by the seafloor ARray Experiment for the Society.

where η, k, and H are wave height, wavenumber, and water depth, respectively. Note that z is downward positive and that the positive y direction is the direction of tsunami propagation. Given that the Earth is electrically homogeneous beneath the flat seafloor, we obtained analytical solutions for Equations 1 and 2 within the ocean layer:

$$\eta(\omega) = \frac{b_z(\omega, z)}{C(\omega, z)}, \text{and} \tag{3}$$

$$C(\omega, z) = C_1 e^{a_s z} + C_2 e^{-a_s z} + \frac{\omega k P}{\sinh(kH)} \cdot \left[i F_Z \cosh[k(z-H)] - F_y \sinh[k(z-H)] \right], \tag{4}$$

where $a_s = \sqrt{k^2 - i\omega\mu_0\sigma_s}$, $a_f = \sqrt{k^2 - i\omega\mu_0\sigma_f}$, and $P = \frac{\sigma_s \mu_0}{k^2 - a_s{}^2}$, where σ_s and σ_f are the conductivity of seawater and the sub-seafloor semi-infinite homogeneous medium, respectively. C_1 and C_2 are given by

$$C_1 = \frac{(k+a_s)\cdot\left[\mathrm{P}k\frac{\omega}{\sinh(kH)}\cdot(kF_y - a_f F_z)\right] - (a_f - a_s)e^{-a_s h}\cdot\left[-\mathrm{P}k^2\cdot(F_y + iF_z)\cdot\left(\frac{\omega}{\tanh(kH)} + \omega\right)\right]}{(k+a_s)(a_f+a_s)e^{a_s h} - (k-a_s)(a_f-a_s)e^{-a_s h}},$$

$$C_2 = \frac{(k-a_s)\cdot\left[\mathrm{P}k\frac{\omega}{\sinh(kH)}\cdot(kF_y - a_f F_z)\right] - (a_f + a_s)e^{a_s h}\cdot\left[-\mathrm{P}k^2\cdot(F_y + iF_z)\cdot\left(\frac{\omega}{\tanh(kH)} + \omega\right)\right]}{(k-a_s)(a_f-a_s)e^{-a_s h} - (k+a_s)(a_f+a_s)e^{a_s h}}.$$

After applying a discrete Fourier transform (DFT) to the magnetic time series data, Equations 3 and 4 can be used to convert the vertical component of the tsunami-generated magnetic field to sea-surface fluctuation at each frequency by using a set of (k,ω) that meets the tsunami dispersion relationship of $\omega^2 = gktanh(kH)$. The inverse DFT of the obtained frequency-domain wave height provides a time series of sea surface fluctuations at an OBEM site.

We used the method above to obtain the sea-level changes resulting from the 2009 Samoa tsunami from the observed tsunami magnetic vertical components at SOC stations by assuming $\sigma_s = 4$ S/m, $\sigma_f = 0.01$ S/m, $F_z = 21{,}181$ nT, and $F_y = 10{,}316$ nT, where F_z and F_y were from the IGRF-11 model of Finlay et al. (2010), in the same manner as Lin et al. (2021). The measured water depths at all SOC stations were used for this conversion. The data-sampling interval was set to 1 min after band-pass filtering for 3–30 min.

SOCs 1–7 and 9 were equipped with OBEM only, and SOC8 was equipped with both OBEM and OBP. Figure 2 compares the time series of the water level at SOC8 converted from OBEM and OBP data. For the hydrostatic pressure data conversion, we assumed that a 1 hPa change in the bottom pressure corresponded to a 1 cm change in the water level. The water level fluctuation estimated from the OBEM data was almost identical to that estimated from the OBP data, indicating that our conversion of tsunami magnetic field data was successful at least for the distant tsunami. However, a difference in background noise levels was found. The background noise levels were 5.2 and 0.5 mm in the root-mean-square (RMS) of water level fluctuations converted from the magnetic field and pressure data, respectively, during the 2 hours before the tsunami arrival. The large background noise in the magnetic-field-derived water level fluctuation was probably caused by the Earth's magnetic field fluctuations of external origin and/or the 0.01 nT resolution of the magnetometer used. OBP observations were highly accurate because short-wavelength water pressure fluctuations caused by wind waves do not affect ocean-bottom pressure, whereas external geomagnetic variations for a period of 5 min can reach even at the deep seafloor of the South Pacific Ocean. Furthermore, the magnetic resolution of 0.01 nT is roughly equivalent to one digit error of 2.27 mm in water level for the ocean depth of 4,806 m at SOC8. In the tsunami inversion analysis, the difference in weight between the OBEM and OBP data was based on the background noise level. Section 3.3 explains in detail how the weights were determined.

Our band-pass filter range (3–30 min) on the OBEM-derived waveforms was narrower than 1–60 min, which Hossen et al. (2018) have applied to the OBP waveforms of the 2009 Samoa tsunami recorded by DART stations. The OBEM-derived waveforms at SOC stations suffered from significant noise in the frequency range of 30–60 min (Figure S1 in Supporting Information S1), presumably due to the earth's magnetic field fluctuation. We inevitably used the narrow filter range. However, no difference between the OBP waveforms filtered by 1–60 and 3–30 min at SOC8 was observed. Hence, the 2009 Samoa tsunami around SOCs did not have a component in the 30–60 min frequency range.

2.2. Ocean Bottom Pressure Data

We downloaded other OBP tsunami data from the DART website. DART data are usually sampled at 15 min intervals; however, this interval is changed to 1 min or 15 s when tsunami events are detected. For our inversion analysis, we used DART data (Figure 1) recorded at sampling rates of either 1 min or 15 s. We

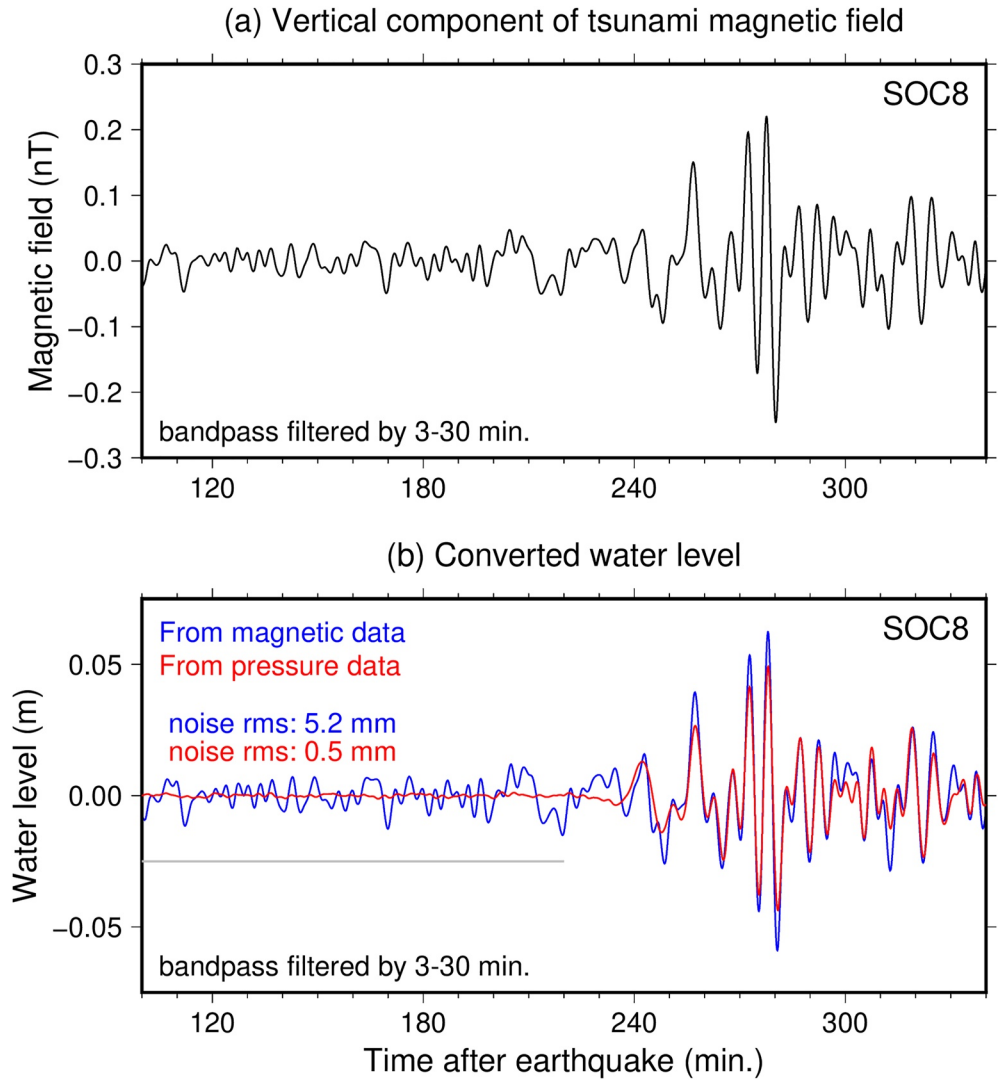

Figure 2. (a) Downward tsunami magnetic component of the 2009 Samoa tsunami recorded at SOC8. (b) Water level fluctuations converted from the tsunami magnetic component (blue) and the OBP data (red). Background noise levels were estimated using data from 2 hr (range represented by the horizontal gray bar) before the arrival of the tsunami.

removed tidal components from the OBP records using the NAO.99b tidal prediction system by Matsumoto et al. (2000). To recover the tsunami components, we applied a 1–60 min band-pass filter similar to that by Hossen et al. (2018). We subsequently used these data sampled at one-minute intervals for our joint inversion with the OBEM data.

3. Method of Finite Fault Slip Inversion

3.1. Configuration of the Two Fault Planes and Subfaults

We assumed that the 2009 Samoa earthquake was a doublet earthquake with the same fault and subfault configurations as those of Hossen et al. (2018). The normal fault plane was modeled as a 150 km × 50 km rectangle striking 315° clockwise and dipping 25° northeast with its upper edge at a depth of 1.4 km. The rake angle was set at −99°. The thrust fault plane was a 175 km × 125 km rectangle with its upper edge at a depth of 1.4 km. The strike, dip, and rake angles were 180°, 29° west, and 90°, respectively. Both fault planes were subdivided into 25 km × 25 km square subfaults. Table S1 in Supporting Information S1 lists the fault parameters for each subfault.

We computed the seafloor crustal deformation for a unit slip on each subfault using the analytical solution for an isotropic, homogeneous, and semi-infinite medium (Okada, 1985). Both the vertical displacement of the seafloor and horizontal displacement of the seafloor slope can lift the water column and initiate a tsunami (Tanioka & Satake, 1996); thus, we included both effects on tsunami generation. We also applied the hydraulic filter postulated by Kajiura (1963) to the calculated seafloor displacement to obtain the initial sea-surface deformation caused by each subfault.

3.2. Calculation of Green's Functions for Tsunamis

Because the OBEM and OBP stations used in this study were deployed on the deep seafloor, the nonlinearity of the first few waves of the 2009 Samoa tsunami can be disregarded; therefore, the use of a linear inversion scheme (Satake, 1987) to estimate fault slip distributions is appropriate. To image the source of the 2009 Samoa tsunami, Hossen et al. (2018) used linear long-wave equations for tsunami waveforms recorded at only a few stations located close to the tsunami source because the governing equations for these calculations do not account for dispersion effects. Tsunami dispersion is evident in data recorded at distant stations (Watada et al., 2014; Zhou et al., 2012). There are two types of dispersion: (a) frequency dispersion, where shorter-wavelength waves are slower than longer-wavelength waves, and (b) dispersion caused by the self-attraction and loading (SAL) effect (Allgeyer & Cummins, 2014; Watada et al., 2014), in which waves with super-long wavelength travel slowly. To derive Green's functions for tsunamis in this study, we used the linearized tsunami equations of Baba et al. (2017), which include both dispersion effects. The governing equations for these calculations are as follows:

$$\frac{\partial M}{\partial t} = -\frac{gH}{R\sin\theta}\frac{\partial \eta}{\partial \varphi} - fN + \frac{H^2}{3R\sin\theta}\frac{\partial}{\partial \varphi}\left[\frac{1}{R\sin\theta}\left(\frac{\partial^2 M}{\partial \varphi \partial t} + \frac{\partial^2 (N\sin\theta)}{\partial \theta \partial t}\right)\right], \tag{5}$$

$$\frac{\partial N}{\partial t} = -\frac{gH}{R}\frac{\partial \eta}{\partial \theta} + fM + \frac{H^2}{3R}\frac{\partial}{\partial \theta}\left[\frac{1}{R\sin\theta}\left(\frac{\partial^2 M}{\partial \varphi \partial t} + \frac{\partial^2 (N\sin\theta)}{\partial \theta \partial t}\right)\right], \text{and} \tag{6}$$

$$\rho_H \frac{\partial(\eta+\xi)}{\partial t} = -\frac{\rho_{ave}}{R\sin\theta}\left[\left(\frac{\partial M}{\partial \varphi} + \frac{\partial (N\sin\theta)}{\partial \theta}\right)\right], \tag{7}$$

where M and N are depth-integrated flow quantities equal to Hv_x and Hv_y, respectively, along longitude ϕ and colatitude θ. Variables v_x and v_y are horizontal water velocities in the x and y directions. H is the at-rest ocean depth, R is the Earth's radius, η is the difference in sea level at elapsed time t from the origin time. g is gravitational acceleration, f is the Coriolis parameter, ξ is the displacement of the seafloor from its at-rest depth H, and ρ_H and ρ_{ave} are seawater density at the seafloor and average seawater density along the vertical profile, respectively. The displacement of the seafloor ξ in Equation 7 was calculated by convolving the following function with the change in ocean depth $(\eta + \xi)$,

$$G(\boldsymbol{r}', \boldsymbol{r}) = G(\alpha) = \frac{-R}{M_e}\sum_{n=0}^{\infty}\left(1 + k'_n - h'_n\right)P_n(\cos\alpha). \tag{8}$$

Equation 8 describes the Earth's elastic response to a unit mass load concentrated at a point on its surface (Vinogradova et al., 2015), where $\boldsymbol{r}$ denotes an arbitrary position on the Earth's surface with the point mass located at $\boldsymbol{r}'$. P_n refers to Legendre polynomials, α is the angular separation between $\boldsymbol{r}'$ and $\boldsymbol{r}$. M_e is the mass of the Earth, and k'_n and h'_n are the elastic loading Love numbers of angular order n.

The initial sea-surface deformation was calculated for each subfault with a rise time of 60 s, and tsunami propagation was subsequently calculated by solving Equations 5–8 on staggered finite-difference grids using a leapfrog scheme. For the dispersion terms (the third term on the right side of Equations 5 And 6), we applied the red-black Gauss-Seidel method. The topographic and bathymetric data used for tsunami computation were obtained from the ETOPO1 data set (Amante & Eakins, 2009) with a spatial grid resolution of 1 arcmin. The integral time was 54,000 s (15 hr) after the earthquake origin time. The time step for tsunami computations was set at 0.1 s to satisfy the stability conditions.

We also performed three sensitivity analyses for our calculations of Green's functions by selectively applying the following governing equations: These analyses are based on

1. Equations 5–8: Linear dispersive wave equations with SAL effect (denoted as LDW + SAL);
2. Equations 5–7 without ξ, ρ_H, and ρ_{ave}—the linear dispersive wave equations (denoted as LDW) only;
3. Equations 5 and 6 without the dispersion terms (the last term of the right-hand side of both equations), together with Equation 7 without ξ, ρ_H, and ρ_{ave}—the linear long-wave equations (denoted as LLW). This replicated the methodology described by Hossen et al. (2018).

3.3. Linear Inversion for Finite Fault Slip

Observed data were used in the following equation to obtain the slip distribution of the 2009 Samoa earthquake.

$$\begin{pmatrix} w\boldsymbol{O}_{EM} \\ \boldsymbol{O}_P \\ \boldsymbol{0} \end{pmatrix} = \begin{pmatrix} w\boldsymbol{G}_{EM} \\ \boldsymbol{G}_P \\ \alpha \boldsymbol{I} \end{pmatrix} \boldsymbol{X}, \tag{9}$$

where the vectors $\boldsymbol{O}_{EM}$ and $\boldsymbol{O}_P$ are the observed sea level displacements converted from the OBEM and OBP data, respectively, during the tsunami. $\boldsymbol{O}_{EM}$ were derived from SOC stations. Although SOC8 was equipped with both OBEM and OBP, only OBEM data were used to evaluate their applicability to tsunami inversion analysis. $\boldsymbol{O}_P$ were derived from DART observations. Matrices $\boldsymbol{G}_{EM}$ and $\boldsymbol{G}_P$ contain the Green's functions for the tsunami computed from the 47 subfaults. Matrix $\boldsymbol{I}$ is the identity matrix for L2-norm regularization to avoid the instability of solution $\boldsymbol{X}$ (the amount of slip on each subfault). A hyper-parameter (α) determined the weight between the observed data and the regularization term (optimized as described in the next paragraph). The weight parameter (w) determined the weight between the observed OBEM and OBP data. Solution $\boldsymbol{X}$ cannot be negative; therefore, we used the nonnegative least-squares algorithm (Lawson & Hanson, 1995) for our inversion.

We used a "leave one station out" cross-validation method to find the optimal value of α, in which for a given value of α, data from one station were excluded from the observational equation, and a temporary inversion solution was obtained. Subsequently, using the temporary solution, we predicted the excluded observed data and calculated the residual. We repeated these inversions, excluding each of the 16 stations, and summed the residuals for all 16 cases. Subsequently, we went through the same process for different values of α to obtain the sum of residuals of those predictions, and used the minimum sum to identify the optimal value of α, which we estimated to be 0.0044 for the 2009 Samoa tsunami data set. Next we used that value with the observed data to obtain the final slip model. The standard deviation of the cross-validation solutions was used as the error of the modeled slip.

The weight value (w) between the OBEM and OBP data was determined based on the background noise levels of the OBEM and OBP data. We repeated the inversions by changing the value of w and elevating the RMS error (RMSE) between the observed and synthetic tsunami waveforms, that is, $\sqrt{\|\boldsymbol{O}_{EM} - \boldsymbol{G}_{EM}\boldsymbol{X}\|/n}$ and $\sqrt{\|\boldsymbol{O}_P - \boldsymbol{G}_P\boldsymbol{X}\|/m}$, where n and m are the numbers of data points. It should be noted that each inversion searched the optimal value of α using the cross-validation method. We chose 0.2 as the optimal value of w. Here, the RMSE of the OBEM data was larger than that of the OBP data by 5 mm, because the observed background noise level of the OBEM data was larger than that of the OBP data by approximately 5 mm (Figure 2).

4. Inversion Results

The maximum amounts of slip estimated by our inversion were 7.0 and 3.5 m on the normal and thrust fault planes, respectively (Figure 3 and Table S1 in Supporting Information S1). Significant slip on the normal fault appeared in the subfaults surrounding the epicenter. The slip area on the thrust fault extended in a north-south direction in the upper part of the fault plane. The calculated seismic moments were 3.74×10^{20} Nm (Mw 7.6) for the normal fault and 5.56×10^{20} Nm (Mw 7.8) for the thrust fault, assuming a rock rigidity of 40 GPa. The total seismic moment was 9.31×10^{20} Nm (Mw 7.9).

We compared the seismic moments and slip distributions with those by Hossen et al. (2018), which was the most accurate published model at the time our investigation started. This model used Green's functions derived from LLW equations and data recorded at neighboring stations. The seismic moments estimated for the normal and thrust faults were comparable to those obtained by Hossen et al. (2018), who estimated seismic moments of 1.18×10^{20} Nm (Mw 7.4) for the normal fault and 7.33×10^{20} Nm (Mw 7.9) for the thrust fault. The slip

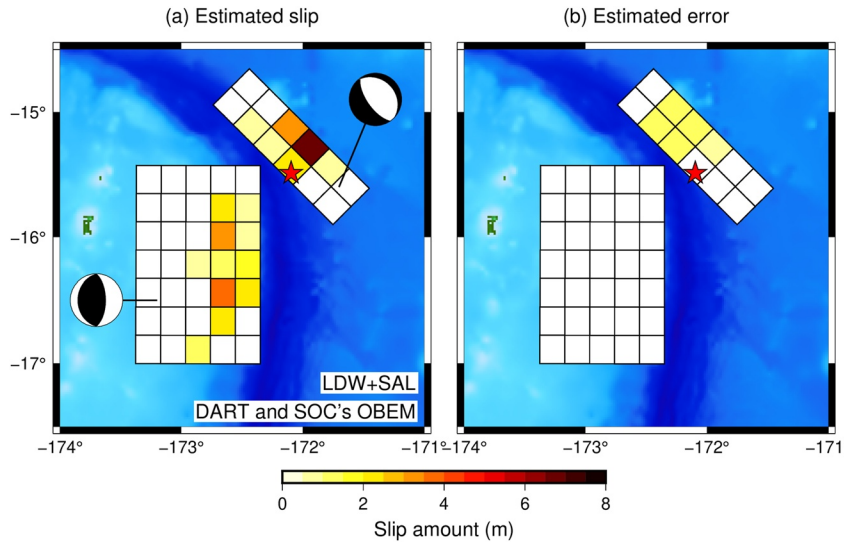

Figure 3. Estimated (a) slip distribution and (b) slip errors on the thrust and normal fault planes of the 2009 Samoa earthquake using data recorded by the OBEMs of the SOCs and DART stations. The hypocenter (red star) determined by U.S. Geological Survey is also shown. The focal mechanisms indicate fault motion assumed in the inversion analysis. The internal squares on each fault plane are the subfaults used in the modeling. LDW, linear dispersive wave equations; SAL, self-attraction and loading effects.

distribution we determined on the normal fault was similar to that of Hossen et al. (2018), whereas for the thrust fault, the east-west width of the slip zone that we determined was narrower, and its position was shifted to the east.

The RMSE between the observed and calculated tsunami waveforms used in the inversion was 6.8 and 11.8 mm for the OBP and OBEM data, respectively. The variance reduction (VR), determined as $1 - \sum (\eta_{cal} - \eta_{obs})^2 / \sum \eta_{obs}{}^2$, was 74% and 56%, respectively (Figure 4). Hossen et al. (2018) used OBP data to estimate a fault slip model that produced an RMSE of 14.2 mm and a VR of 19%. Thus, our slip distribution yielded better reproducibility of the observed tsunami waveforms than that of Hossen et al. (2018).

A retrieval resolution test was performed to verify the reliability of the inversion solutions. For this test, we used the obtained slip distribution to calculate the synthetic tsunami waveforms at each station using the method described in Section 3.2. Then, we added Gaussian noise corresponding to the observed background noise level with standard deviations of 5.0 and 0.5 mm for the OBEM and OBP, respectively, to the calculated tsunami waveforms to obtain pseudo-observation data. We inverted these data using the method described in Section 3.3 in an attempt to recover the assumed slip pattern. A good match with the assumed slip pattern indicated that the inversion solution was reliable (Figure S2 in Supporting Information S1).

We used checkerboard slip patterns to explore the spatial resolution of the estimated slip distributions. A checkerboard slip distribution was initially constructed using pseudo-slip amounts of 2 and 0 m in alternating 50 km × 50 km subfaults. We created synthetic tsunami waveforms with background noise and performed an inversion analysis using pseudo-observation data. Checkerboard slip patterns were mostly retrieved, although some subfaults showed slips where there should have been no slip (Figure S3 in Supporting Information S1). For the checkerboard slip pattern in alternating 25 km × 25 km subfaults, the retrieved slips did not match the original checkerboard pattern. Thus, these results indicate that the data set used in our study can resolve slips of 2 m on 50 km × 50 km subfaults or greater on the fault planes of the 2009 Samoa earthquake.

5. Discussion

5.1. Estimated Magnitude and Rupture Difference

The earthquake magnitudes of the normal and thrust faults obtained by this study (Mw 7.6 and 7.8, respectively) were similar to those obtained by Hossen et al. (2018) (Mw 7.4 and 7.9, respectively), who also used the DART tsunami data to estimate it. However, these are smaller than those estimated from seismic wave analysis:

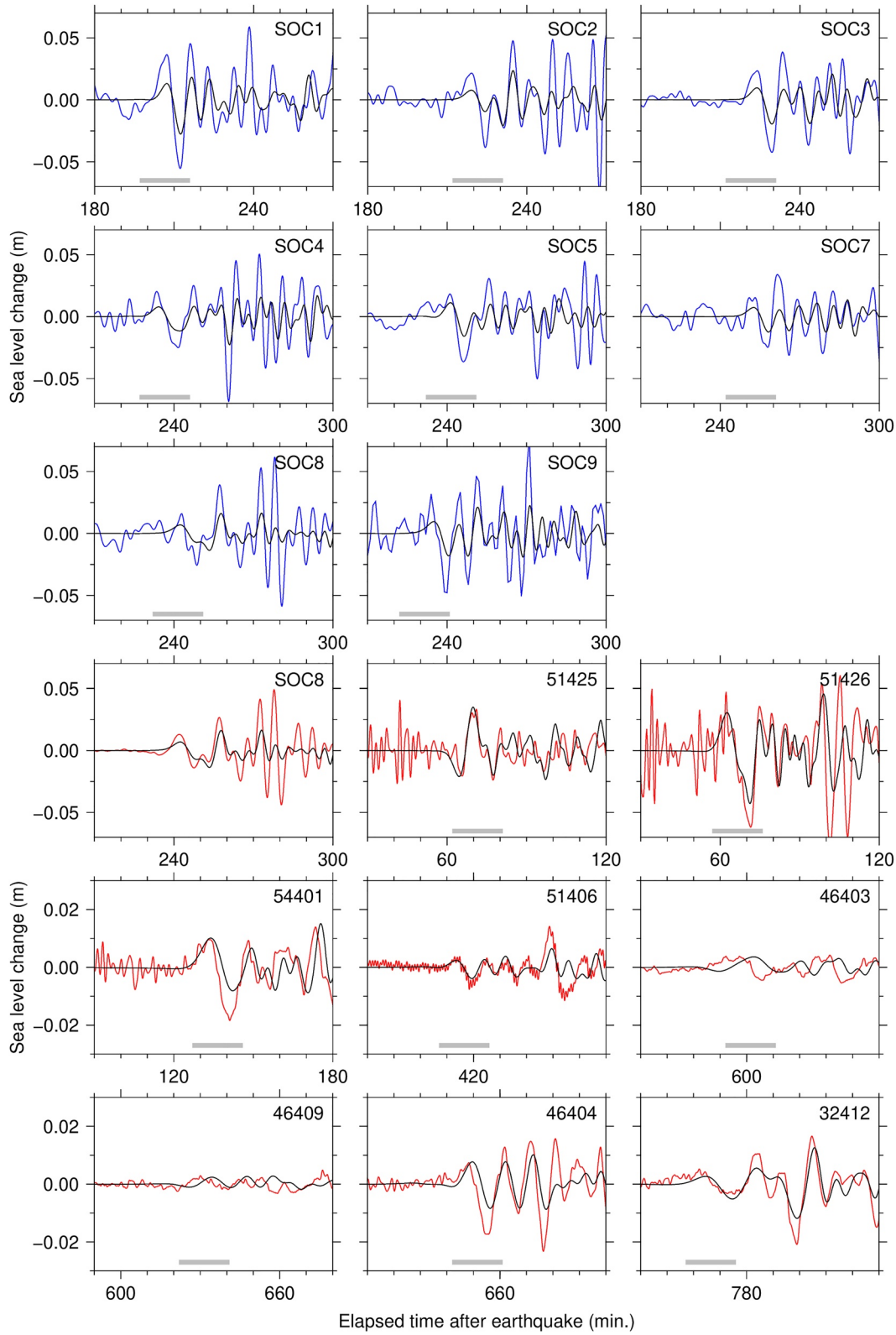

Figure 4. Comparison of observed and synthetic tsunami waveforms at SOC and DART stations (see Figure 1 for locations). Observed tsunami waveforms derived from OBEM and OBP are in blue and red, respectively. Waveforms in black are calculated from the slip model shown in Figure 3a. Horizontal gray bars under the waveforms indicate the time windows used in the inversions as containing the first tsunami waves.

Beavan et al. (2010) estimated Mw 7.9 and Mw 8.0, while Lay et al. (2010) estimated Mw 8.1 and Mw 8.0, for the normal and thrust faults, respectively. Lay et al. (2010) further divided the Mw 8.0 thrust rupture into two sub-ruptures (both Mw 7.8). Nealy and Hayes (2015) obtained Mw 8.0 for both the normal and thrust faults and in Fan et al. (2016), these were Mw 8.0 and Mw 8.1, respectively. Although the estimated magnitude in the tsunami inversion varies depending on the assumed rigidity, our estimations were significantly smaller, even after considering the range of rigidity. The tsunami waveform comparison in Figure 4 shows that the amplitude of the tsunami waveforms synthesized from our slip model is smaller than that of the observation, which is specifically clear at the SOC stations. Therefore, the real magnitude of the 2009 Samoa earthquake must be greater than our estimations. This underestimation of the earthquake magnitude may be due to the incompleteness of the tsunami inversion analysis applied in this study. Specifically, the fault-plane geometry may have room for improvement. We used an analytical solution of a semi-infinite homogeneous elastic body (Okada, 1985) for crustal deformation calculations. However, the subduction zone has a complex crustal structure with varying stiffness strength. Although cross-validation is commonly used to determine the weight between the observed data and the regularization term, it may not be suitable for tsunami inversion analysis. Answering this question is challenging, and we will continue to investigate it.

The 2009 Samoa slip occurred first on the normal fault, followed shortly after by the slip on the thrust fault. Investigating the sequential ruptures of earthquakes is essential to understand the mechanism of earthquake occurrence. Regarding the delay between the ruptures on the normal and thrust faults, previous reports estimated the interval between the two events to be less than 1 minute (Fan et al., 2016; Lay et al., 2010; Nealy & Hayes, 2015). In our analysis, we treated the ruptures of the normal and thrust faults simultaneously because the sampling interval for the OBEM data was 60 s; thus, we could not discriminate a time difference between the two ruptures shorter than 60 s. However, a test delaying the rupture of the thrust fault by 60 s shifted the thrust fault's slip to the east because many observation points were located on the east side of the earthquake (Figure S4 in Supporting Information S1). The slip moved closer to the observation points, explaining the tsunami arrival time (i.e., the rupture time difference). The tsunami propagation velocity around the tsunami source was 221 m/s (approximately 13 km/min) at a water depth of 5,000 m. The width of the subfault is 25 km, and its dip is 29°. A rupture delay of 2 min would shift the slip from one subfault to the east. Therefore, a trade-off was observed between the slip location and the rupture time difference in the 2009 Samoa tsunami inversion analysis.

5.2. OBEM Data as an Alternative to OBP Data

Typically, OBPs are used for tsunami observation in the deep ocean. OBP tsunami observations are accurate because the water pressure changes caused by wind waves do not reach the deep ocean bottom. In addition, the dominant frequency of the tsunami differs from that of wind waves. Accordingly, tsunami observations can be performed in a quiet pressure environment at the ocean bottom. As shown in Figure 2, the background noise level was approximately 0.5 mm, which means that a tsunami with an amplitude of a few millimeters can be detected by OBPs. However, OBP observations are sparse in oceans and typically insufficient. Spatially continuous observations are possible using satellite radar; however, the satellite must remain in the air during tsunami propagation. The lack of observational data is a fundamental problem in fault model estimation using tsunami inversion. In this study, we focused on tsunami observations by OBEM as a solution for this problem. The background noise level was approximately 5 mm for the water fluctuations converted from the OBEM data using the analytical solution, which should be able to detect a tsunami of a few centimeters propagating over the ocean. OBEMs can be used to observe tsunamis caused by earthquakes with magnitudes of 8 and larger, such as the 2009 Samoa earthquake, although they may not be suitable for detecting microtsunamis.

TIARES had nine seafloor stations (SOC1–9); fortunately, SOC8 was equipped with both OBEM and OBP. We also estimated the fault slip distribution of the Samoa earthquake using the same method as described in Section 3, without using the OBEM data of SOC and instead using the OBP of the SOC8 and DART stations. We found that the slip distribution (Figure 5) was almost the same as that obtained using the DART and SOC OBEMs (Figure 3). Our results demonstrate that the OBEM data can be an alternative option to the OBP data for tsunami observations in the ocean.

In Equation 1, the tsunami-generated magnetic field is a function of the horizontal velocity field of seawater movements. OBEM observations may also retrieve the horizontal velocity of seawater movement caused by tsunamis, which cannot be obtained from OBP observations. Although analytical methods to convert the

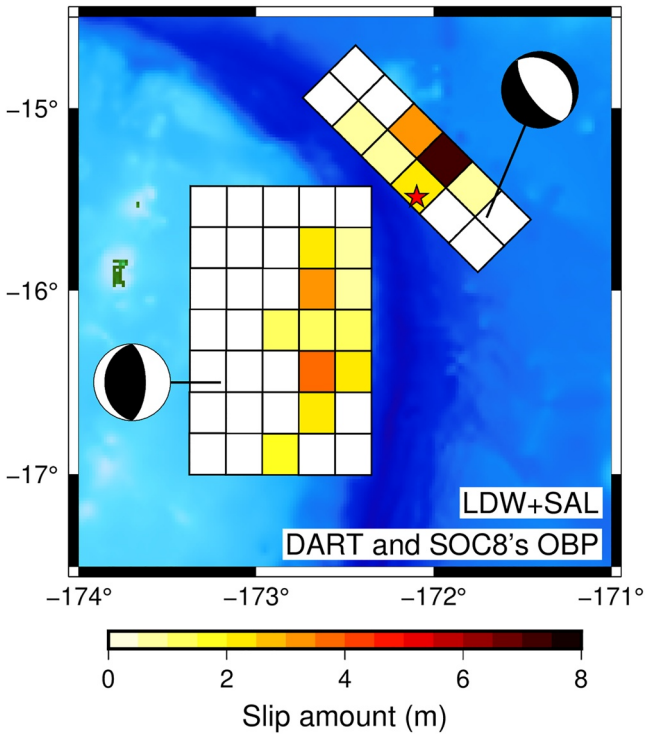

Figure 5. Estimated slip distribution on the thrust and normal fault planes of the 2009 Samoa earthquake using data recorded by the OBP of the SOC8 and DART stations. See Figure 3 for the other explanations.

tsunami magnetic field to water level fluctuations exist, conversion to horizontal velocity fields has not yet been accomplished. This is a challenging task that we aim to solve in our upcoming study. Nonetheless, the present computational resource is sufficient to perform a three-dimensional magnetic field numerical simulation using the velocity field calculated from tsunami numerical simulation (e.g., Lin et al., 2021; Minami et al., 2017). Therefore, it is now feasible to use the OBEM data for tsunami source inversions more directly by preparing Green's functions for the tsunami magnetic field instead of Green's functions for the tsunami wave field. This way, we will be able to use both the vertical and horizontal magnetic components of tsunami origin.

5.3. Factors Governing the Slip Distribution

The slip distribution we determined on the normal fault was similar to that of Hossen et al. (2018), whereas for the thrust fault, the east–west width of the slip zone that we determined was narrower, and its position was shifted to the east. The combined effect of the OBEM data and advanced tsunami calculation methods altered the slip distribution significantly. Therefore, we performed additional inversion analyses to understand the effects of different governing equations and combinations of input observational data on the slip distribution (Figure 6). Based on the sensitivity tests, the following outcomes were obtained:

1. Inversion using data from only three neighboring DART stations with Green's functions derived from the LLW equations (Figure 6a) showed a slip area close to the center of the thrust fault, similar to that by Hossen et al. (2018).
2. Inversion using data from the three neighboring DART stations but with Green's functions derived from the LDW equations (Figure 6b) provided a slip distribution similar to that in point (1) because the dispersive effect was negligible in the tsunami waveforms recorded at the stations neighboring the source.
3. Inversion using data from three neighboring DART stations and the OBEM data from eight SOC stations with Green's functions derived from the LDW equations significantly changed the slip distribution (Figure 6c). The maximum slip was estimated to be approximately 15 m. The slip area extends in the north-south direction on the thrust fault. We attributed these changes to shorter-wavelength components in the tsunami data recorded by the TIARES stations. However, the slip distribution appeared unrealistic because of large undulations. Based on a comparison with the results in point (4), we believe that the LDW tsunami propagation model was insufficient for simulating the tsunami waveforms recorded at the OBEM stations.
4. Inversion using data from the same set of stations as in point (3) and Green's functions derived from the LDW + SAL equations estimated a slip model (Figure 6d) similar to the final model shown in Figure 3a. The dimensions of the slip area were approximately 50 km × 50 km on the normal fault and 75 km × 150 km on the thrust fault. This inversion analysis eliminated the disorder in the slip distribution that appeared in point (3).

These results indicate that including data from the OBEM stations east of the tsunami source constrained the east-west extent of the slip area on the thrust fault of the 2009 Samoa earthquake, and that the use of the LDW equations considering the SAL effect stabilized the inversion result.

In this study, the magnetic data recorded by OBEMs and the converted sea level variations were effective for analyzing dispersive tsunamis. The significance of dispersion effects in the SOC magnetic data during the 2009 Samoa event has been recognized in a study that utilized wavelet analysis (see Figure 11 of Schnepf et al., 2017), which observed that long-period magnetic variations preceded the shorter ones at specific sites.

6. Conclusions

Although Kawashima and Toh (2016) developed a fault slip model by inversion using only OBEM data, this study is the first to use both OBEM and OBP data to generate an earthquake source model. Furthermore, our use

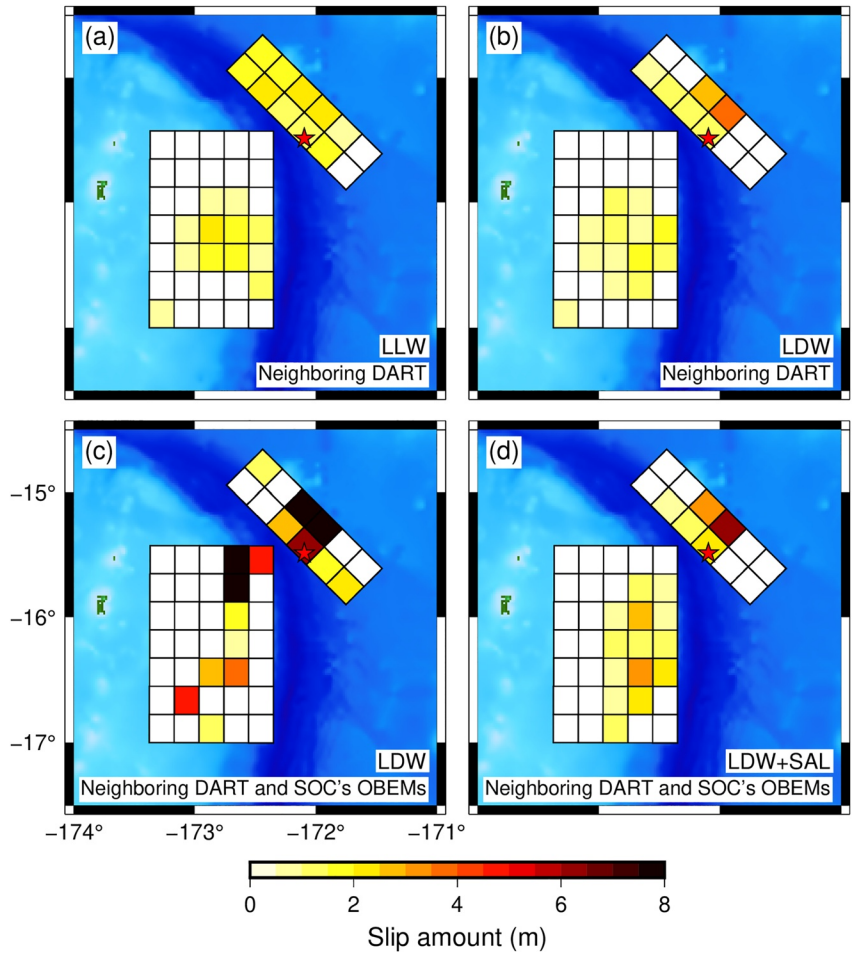

Figure 6. Inversion results for different combinations of the governing equations and OBP and OBEM stations included. Slip distributions were inverted by (a) LLW Green's functions and neighboring DART stations, (b) LDW Green's functions, neighboring DART stations, (c) LDW Green's functions, neighboring DART stations, and SOC's OBEM stations, and (d) LDW + SAL Green's functions, neighboring DART stations, and SOC's OBEM stations. LLW, linear long-wave equations; LDW, linear dispersive wave equations; SAL, self-attraction and loading effects. See Figure 1 for the station locations.

of the linear dispersive wave equation incorporating of the SAL effect provides a new model for the 2009 Samoa tsunami. The modeled slip distributions presented herein provide more accurate predictions of the observed data than those of previous studies. The most important findings of our study are as follows:

1. The background noise level of the converted water-level fluctuations from the OBEM data was approximately 5 mm; therefore, we were able to detect a tsunami with an amplitude larger than a few centimeters.
2. Tsunami waveforms derived from OBEM data can be easily incorporated in conventional tsunami waveform inversion schemes.
3. Dealing with both the effects of frequency dispersion and SAL was important in the finite fault inversion of tsunami waveforms recorded at SOC stations.
4. Compared with the results of previous studies, our doublet slip model effectively reproduced the 2009 Samoa tsunami waveforms recorded at both OBP and OBEM, and found that the slip area modeled on the thrust fault was compressed in the east–west direction and was shifted eastward toward the shallow plate interface.

The next challenge lies in utilizing the horizontal components of the tsunami magnetic field observed through OBEM in the tsunami inversion. Although an analytical equation was not found for converting the horizontal tsunami magnetic field to the tsunami wave field, we were able to accurately calculate tsunami magnetic fields through large-scale numerical simulations. Thus, investigating how much the horizontal component of the tsunami magnetic field contributes to improving the earthquake source estimation is crucial.

Data Availability Statement

All the data used in this study are publicly accessible. The DART data are available from the NOAA Pacific Marine Environmental Laboratory at https://nctr.pmel.noaa.gov/Dart/. The OBEM tsunami data were obtained from the Supporting Information published by Lin et al. (2021). Bathymetric and topographic data for ETOPO1 are available at https://www.ngdc.noaa.gov/mgg/global/. The tsunami software used, JAGURS (Baba et al., 2017), is available from the online repository at http://dx.doi.org/10.5281/zenodo.3737816. The NAO.99b tidal prediction system can be downloaded from https://www.miz.nao.ac.jp/staffs/nao99/index_En.html.

Acknowledgments

We would like to thank Dr. Jakir Hossen and Dr. Aditya Gusman for providing the subfault configurations used in their 2018 analysis of the 2009 Samoa earthquake. We also express our sincere thanks to Dr. Hiroko Sugioka and Dr. Kiyoshi Baba for having provided the ocean-bottom pressure and magnetic data in the TIARES area, respectively. We thank two anonymous reviewers whose constructive feedback improved the manuscript. We also thank the associate editor, Dr. Satoshi Ide for editing the manuscript. This work was supported by KAKENHI Grants from the Japan Society for the Promotion of Science (Numbers JP20H00294, JP22H01308, and JP22H01742) and by the Earthquake Research Institute, University of Tokyo (ERI JURP 2022-S-B101). For our tsunami calculations, we used the FUJITSU Supercomputer PRIMEHPC FX1000 and the FUJITSU Server PRIMERGY GX2570 (Wisteria/BDEC-01) at the Information Technology Center, The University of Tokyo, and on the Earth Simulator at the Japan Agency for Marine-Earth and Technology. We used GMT Version 5.4.5 (Wessel et al., 2013) for data handling and drawing figures in the manuscript.

References

Allgeyer, S., & Cummins, P. R. (2014). Numerical tsunami simulation including elastic loading and seawater density stratification. *Geophysical Research Letters*, *41*(7), 2368–2375. https://doi.org/10.1002/2014GL059348

Amante, C., & Eakins, B. W. (2009). *ETOPO1 1 arc-minute global relief model: Procedures, data sources and analysis*. NOAA Technical Memorandum NESDIS NGDC-24. National Geophysical Data Center, NOAA. https://doi.org/10.7289/V5C8276M

Baba, T., Allgeyer, S., Hossen, J., Cummins, P. R., Tsushima, H., Imai, K., et al. (2017). Accurate numerical simulation of the far-field tsunami caused by the 2011 Tohoku earthquake, including the effects of Boussinesq dispersion, seawater density stratification, elastic loading, and gravitational potential change. *Ocean Modelling*, *111*, 46–54. https://doi.org/10.1016/j.ocemod.2017.01.002

Beavan, J., Wang, X., Holden, C., Wilson, K., Power, W., Prasetya, G., et al. (2010). Near-simultaneous great earthquakes at Tongan megathrust and outer rise in September 2009. *Nature*, *466*(7309), 959–963. https://doi.org/10.1038/nature09292

Bosserelle, C., Williams, S., Cheung, K. F., Lay, T., Yamazaki, Y., Simi, T., et al. (2020). Effects of source faulting and fringing reefs on the 2009 South Pacific Tsunami inundation in southeast Upolu, Samoa. *Journal of Geophysical Research: Oceans*, *125*(12), e2020JC016537. https://doi.org/10.1029/2020JC016537

Duputel, Z., Kanamori, H., Tsai, V. C., Rivera, L., Meng, L., Ampuero, J.-P., & Stock, J. M. (2012). The 2012 Sumatra great earthquake sequence. *Earth and Planetary Science Letters*, *351–352*, 247–257. https://doi.org/10.1016/j.epsl.2012.07.017

Fan, W., Shearer, P. M., Ji, C., & Bassett, D. (2016). Multiple branching rupture of the 2009 Tonga-Samoa earthquake. *Journal of Geophysical Research: Solid Earth*, *121*(8), 5809–5827. https://doi.org/10.1002/2016JB012945

Faraday, M. (1832). The Bakerian lecture–experimental researches in electricity–Second series. *Philosophical Transactions of the Royal Society of London, Series A: Physical Sciences and Engineering*, *122*, 163–194. https://doi.org/10.1098/rstl.1832.0007

Finlay, C. C., Maus, S., Beggan, C. D., Hamoudi, M., Lowes, F. J., Olsen, N., & Thébault, E. (2010). Evaluation of candidate geomagnetic field models for IGRF-11. *Earth Planets and Space*, *62*(10), 787–804. https://doi.org/10.5047/eps.2010.11.005

Fritz, H. M., Borrero, J. C., Synolakis, C. E., Okal, E. A., Weiss, R., Titov, V. V., et al. (2011). Insights on the 2009 South Pacific tsunami in Samoa and Tonga from field surveys and numerical simulations. *Earth-Science Reviews*, *107*(1–2), 66–75. https://doi.org/10.1016/j.earscirev.2011.03.004

Hossen, M. J., Gusman, A. R., Satake, K., & Cummins, P. R. (2018). An adjoint sensitivity method applied to time reverse imaging of tsunami source for the 2009 Samoa earthquake. *Geophysical Research Letters*, *45*(2), 627–636. https://doi.org/10.1002/2017GL076031

Ichihara, H., Hamano, Y., Baba, K., & Kasaya, T. (2013). Tsunami source of the 2011 Tohoku earthquake detected by an ocean-bottom magnetometer. *Earth and Planetary Science Letters*, *382*, 117–124. https://doi.org/10.1016/j.epsl.2013.09.015

Kajiura, K. (1963). The leading wave of a tsunami. *Bulletin of the Earthquake Research Institute*, *41*, 535–571. https://repository.dl.itc.u-tokyo.ac.jp/record/33711/files/ji0413004.pdf

Kawashima, I., & Toh, H. (2016). Tsunami-generated magnetic fields may constrain focal mechanisms of earthquakes. *Scientific Reports*, *6*(1), 28603. https://doi.org/10.1038/srep28603

Lawson, L., & Hanson, J. (1995). Solving least squares problems. *Classics in Applied Mathematics*, *15*, 340. https://doi.org/10.1137/1.9781611971217

Lay, T., Ammon, C. J., Kanamori, H., Rivera, L., Koper, K. D., & Hutko, A. R. (2010). The 2009 Samoa-Tonga great earthquake triggered doublet. *Nature*, *466*(7309), 964–968. https://doi.org/10.1038/nature09214

Lin, Z., Toh, H., & Minami, T. (2021). Direct comparison of the tsunami generated magnetic field with sea level change for the 2009 Samoa and 2010 Chile tsunamis. *Journal of Geophysical Research: Solid Earth*, *126*(11), e2021JB022760. https://doi.org/10.1029/2021JB022760

Matsumoto, K., Takanezawa, T., & Ooe, M. (2000). Ocean tide models developed by assimilating TOPEX/POSEIDON altimeter data into hydrodynamical model: A global model and a regional model around Japan. *Journal of Oceanography*, *56*(5), 567–581. https://doi.org/10.1023/A:1011157212596

Minami, T., Schnepf, N. R., & Toh, H. (2021). Tsunami-generated magnetic fields have primary and secondary arrivals like seismic waves. *Scientific Reports*, *11*(1), 2287. https://doi.org/10.1038/s41598-021-81820-5

Minami, T., Toh, H., Ichihara, H., & Kawashima, I. (2017). Three-dimensional time domain simulation of tsunami-generated electromagnetic fields: Application to the 2011 Tohoku earthquake tsunami. *Journal of Geophysical Research: Solid Earth*, *122*(12), 9559–9579. https://doi.org/10.1002/2017JB014839

Nealy, J. L., & Hayes, G. P. (2015). Double point source W-phase inversion: Real-time implementation and automated model selection. *Physics of the Earth and Planetary Interiors*, *249*, 68–81. https://doi.org/10.1016/j.pepi.2015.09.005

Okada, Y. (1985). Surface deformation due to shear and tensile faults in a half space. *Bulletin of the Seismological Society of America*, *75*(4), 1135–1154. https://doi.org/10.1785/bssa0750041135

Okal, E. A., Fritz, H. M., Synolakis, C. E., Borrero, J. C., Weiss, R., Lynett, P. J., et al. (2010). Field survey of the Samoa tsunami of 29 September 2009. *Seismological Research Letters*, *81*(4), 577–591. https://doi.org/10.1785/gssrl.81.4.577

Satake, K. (1987). Inversion of tsunami waveforms for the estimation of a fault heterogeneity: Method and numerical experiments. *Journal of Physics of the Earth*, *35*(3), 241–254. https://doi.org/10.4294/jpe1952.35.241

Schnepf, N. R., Manoj, C., An, C., Sugioka, H., & Toh, H. (2017). Time–frequency characteristics of tsunami magnetic signals from four Pacific Ocean events. *Global Tsunami Science: Future Times*, *I*, 3935–3953. https://doi.org/10.1007/978-3-319-55480-8_14

Suetsugu, D., Shiobara, H., Sugioka, H., Ito, A., Isse, T., Kasaya, T., et al. (2012). TIARES Project—Tomographic investigation by seafloor array experiment for the society hotspot. *Earth Planets and Space*, *64*(4), i–iv. https://doi.org/10.5047/eps.2011.11.002

Sugioka, H., Hamano, Y., Baba, K., Kasaya, T., Tada, N., & Suetsugu, D. (2014). Tsunami: Ocean dynamo generator. *Scientific Reports*, *4*(1), 3596. https://doi.org/10.1038/srep03596

Tanioka, Y., & Satake, K. (1996). Tsunami generation by horizontal displacement of ocean bottom. *Geophysical Research Letters*, *23*(8), 861–864. https://doi.org/10.1029/96GL00736

Toh, H., Satake, K., Hamano, Y., Fujii, Y., & Goto, T. (2011). Tsunami signals from the 2006 and 2007 Kuril earthquakes detected at a seafloor geomagnetic observatory. *Journal of Geophysical Research*, *116*(B2), B02104. https://doi.org/10.1029/2010JB007873

Tyler, R. H. (2005). A simple formula for estimating the magnetic fields generated by tsunami flow. *Geophysical Research Letters*, *32*(9), L09608. https://doi.org/10.1029/2005GL022429

Vinogradova, N. T., Ponte, R. M., Quinn, K. J., Tamisiea, M. E., Campin, J.-M., & Davis, J. L. (2015). Dynamic adjustment of the ocean circulation to self-attraction and loading effects. *Journal of Physical Oceanography*, *45*(3), 678–689. https://doi.org/10.1175/JPO-D-14-0150.1

Watada, S., Kusumoto, S., & Satake, K. (2014). Traveltime delay and initial phase reversal of distant tsunamis coupled with the self-gravitating elastic Earth. *Journal of Geophysical Research: Solid Earth*, *119*(5), 4287–4310. https://doi.org/10.1002/2013JB010841

Wessel, P., Smith, W. H. F., Scharroo, R., Luis, J. F., & Wobbe, F. (2013). Generic mapping tools: Improved version released. *EOS Trans., AGU*, *94*(45), 409–410. https://doi.org/10.1002/2013eo450001

Zhang, L., Baba, K., Liang, P., Shimizu, H., & Utada, H. (2014). The 2011 Tohoku tsunami observed by an array of ocean bottom electromagnetometers. *Geophysical Research Letters*, *41*(14), 4937–4944. https://doi.org/10.1002/2014GL060850

Zhou, H., Wei, Y., & Titov, V. V. (2012). Dispersive modeling of the 2009 Samoa tsunami. *Geophysical Research Letters*, *39*(16), L16603. https://doi.org/10.1029/2012GL053068